Article

Analysis of Multi-Objective Optimization Design of Interior Double Radial and Tangential Combined Magnetic Pole Permanent Magnet Drive Motor for Electric Vehicles

Shilun Ma *, **Keqi Chen and Qi Zhang**

School of Automobile and Transportation, Tianjin University of Technology and Education, Tianjin 300222, China; 13187651965@163.com (K.C.); zq532128@163.com (Q.Z.)

* Correspondence: 18698008183@163.com; Tel.: +86-18698008183

Abstract: A new type of interior combined pole permanent magnet drive motor is proposed in this paper, which aims to improve the power and comfort of electric vehicles. In view of the complex magnetic circuit structure and rich harmonic magnetic field of the motor, the initial magnetic pole parameters of the rotor are determined by the equivalent magnetic circuit method. Then, aiming at the complex magnetic circuit and rich harmonic magnetic field, a multi-objective optimization method based on the Taguchi method and response surface method is proposed to reduce the cogging torque, high harmonic content in air gap magnetic flux density and increase the output torque. Based on the finite element analysis of the electromagnetic performance of the new type interior combined magnetic pole permanent magnet drive motor before and after optimization, it can be seen that the improved rotor structure can effectively reduce the torque ripple and increase the torque density. Finally, a prototype was developed and experiments were conducted, and experimental results verified the correctness of the proposed multi-objective optimization algorithm.

Keywords: electric vehicle; interior combined magnetic pole; drive motor; Taguchi method; response surface method

1. Introduction

The development of traditional internal combustion engine vehicles has caused two major problems: energy depletion and environmental pollution. Electric vehicles have become a hot research and development topic for governments and scholars around the world due to their advantages of low pollution and zero emissions. However, as one of the key parts of electric vehicles, the output characteristics of the drive motor directly determine the overall performance of electric vehicles [1–3]. With the increasing pursuit of driving comfort and power, the development of electric drive systems with high performance, high efficiency and high torque density has become an important way to improve the power performance and driving range of electric vehicles [4,5]. At present, the permanent magnet drive motor used in electric vehicles is mostly an interior single magnetic pole structure, and the distribution of magnetic field lines is not uniform, resulting in the obvious depression of the back electromotive force waveform, high harmonic content and large motor loss [6,7]. In recent years, how to improve the torque density of the permanent magnet drive motor and reduce torque ripple has attracted the attention of scholars at home and abroad [8,9].

Generally, the methods to improve torque density and reduce torque ripple can be divided into motor topology innovation and optimization of motor structure parameters. From the perspective of structural innovation. Reference [10] adopts fractional slot winding to effectively reduce higher harmonics and weaken the cogging torque, thus restraining the torque ripple of the permanent magnet motor. Reference [11], through the design of an asymmetrical rotor pole, the pulsation of permanent magnet torque, found that reluctance

torque and cogging torque can be suppressed simultaneously, but the manufacturing process is complicated, and the torque density of the motor will be reduced. Studies [12,13] propose a stator sectionalized interior tangential magnetic field permanent magnet drive motor, which shortens the armature winding end length and improves the torque density, but the sinusoidal trend of the output waveform of the back electromotive force is poor, resulting in large torque fluctuation. Study [14] proposed a tangential magnetic field hybrid pole permanent magnet motor for electric vehicles, which uses the reasonable design of ferrite and NdFeb to reduce the development cost and cogging torque, but at the same time reduces the magnetic flux density of the air gap and output torque. In addition to the improvement of the motor structure, the design parameters of the motor can also be determined by an optimization algorithm, so as to improve the motor's electromagnetic performance. The traditional optimization methods mostly use a single objective for optimization, which not only requires tedious calculation steps and a long development time but also the mutual influence between design parameters is generally ignored, making it difficult to obtain the optimal parameters [15–17]. Study [18] takes high torque density as a single optimization objective for the flux-switched permanent magnet motor, selects parameters such as pole arc coefficient and magnetization thickness of permanent magnets for analysis, and uses finite element analysis to repeatedly adjust structural parameters based on single parameter scanning method to design the motor. The performance capability of this method in multi-parameter interaction, multi-indicator optimization, and global optimization is relatively not particularly outstanding. In study [19], when combining the genetic algorithm and simulated annealing algorithm theory, the flux linkage of the double-stator permanent magnet motor is optimized and analyzed. Although this method can accurately obtain the optimal structural dimension parameters, its optimization process is slow, time-consuming and low efficiency. Study [20] introduced an objective function to modify the multi-objective optimization design method and the maximum value is obtained using the orthogonal test method. Latin-Hypercube, a genetic algorithm, and the simulated annealing algorithm NSGA-II, have good global search ability, but could not fully realize the adaptive genetic optimization [21,22].

In summary, multi-objective optimization algorithms have been widely applied in the design of traditional single-pole permanent magnet motors. Although typical prediction models have good nonlinear approximation ability and strong generalization ability, such models have lower prediction accuracy and larger prediction errors when trained without intelligent optimization algorithms. Some algorithms have strong global search capabilities, but their convergence speed is slow and optimization efficiency is low. Therefore, there is currently no mature method for the multi-objective optimization of the interior combined magnetic pole of permanent magnet motors. In this paper, a new type of permanent magnet drive motor for electric vehicles with a dual radial and tangential interior combination magnetic pole structure (IDRTPMDM) is proposed. Since the combined magnetic pole is composed of multiple magnetic poles, its structure is relatively complex, which increases the number of variables to be considered in the optimization analysis process, the cross-influence on the optimization goal further increases the difficulty of motor optimization and design. On the other hand, the design and analysis of the motor is a complex multi-dimensional overall optimization process, involving electromagnetic torque, torque fluctuation, air gap magnetic density and other optimization objectives. It is very tedious to obtain the best performance of the motor by using the traditional optimization design method [23–25]. Therefore, in order to improve the output torque and reduce the torque ripple as optimization objectives, a new multi-objective optimization method is proposed to give full play to the advantages of different optimization methods, decompose the combined magnetic pole design, and the optimal value of the motor can be obtained accurately. The electromagnetic performance of the motor before and after optimization is simulated by the finite element method, the prototype is made, the experimental platform is built, and the experimental test is carried out. Both theoretical analysis and experimental results show that the optimization design method can meet the high-performance optimization

design requirements of this type of interior combined magnetic pole permanent magnet drive motor.

2. Motor Structure and Working Principle

The structure of IDRTPMDM is shown in Figure 1. Each magnetic pole on the rotor structure is composed of tangential magnetic field rectangular permanent magnet (TRPM), radial magnetic field rectangular permanent magnet (RRPM) and semi-circular radial magnetic field permanent magnet (SRPM). The magnet flux concentration effect is generated between adjacent TRPM to increase the output torque. The RRPM and the SRPM are set on the d-axis to form a series magnetic circuit, which increases improved saliency ratio and maximum speed of the constant power range of the motor. In addition, there is an anchor magnetic barrier between the RRPM and the TRPM, which effectively reduces the magnetic leakage coefficient and improves the utilization rate of permanent magnet material. In this paper, SRPM is innovationally embedded between adjacent TRPM, which makes full use of the limited space of the rotor core to increase the flux of air gap, improve magnetic circuit guidance and high-efficiency interval distribution, and reduce the torque ripple. To make up for the depression of the back electromotive force waveform, reduce high-order harmonic content, and reduce torque ripple. In addition, considering the limit of peak speed and switching frequency, a rotor with eight magnetic poles is adopted, and the stator adopts a 24-slot integer slot winding form. The structure diagram of IDRTPMDM is shown in Figure 1. The corresponding main technical indicators of the permanent magnet drive motor are shown in Table 1.
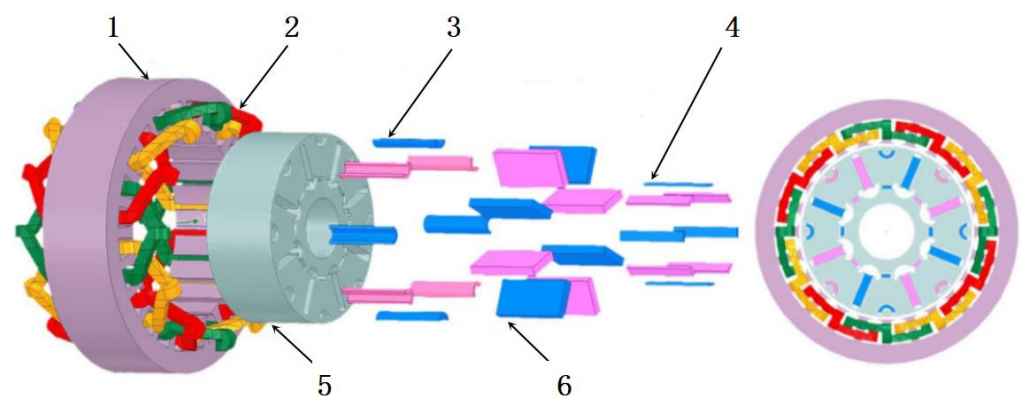

Figure 1. The structure diagram of IDRTPMDM. 1. Stator core; 2. Armature winding; 3. SRPM; 4. RRPMt; 5. Rotor core; 6. TRPM.

Table 1. Main performance parameters of IDRTPMDM.

Parameter	Value	Parameter	Value
Rated power (kW)	3	Rated voltage (V)	60
Rated speed (r/min)	3000	Number of slots/poles	24/8
Outer diameter of stator (mm)	145	Inner diameter of stator (mm)	106
Outer diameter of rotor (mm)	105	Axial length (mm)	60

3. Analysis of Magnetic Pole Parameters Based on EMC Method

The model of IDRTPMDM is established by using the equivalent magnetic circuit method (EMC), which consists of two parallel magnetic flux paths, one is the closed magnetic path formed by TRPM through the rotor core, air gap, stator teeth, stator yoke and stator teeth, and the other is the closed magnetic path formed by two RRPMs in series with each other. As shown in Figure 2, the magnetic flux path diagram of the permanent magnet drive motor with embedded radial and tangential parallel magnetic circuit and its EMC model is shown in Figure 3.
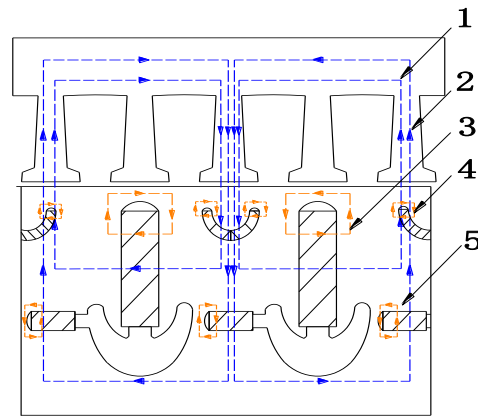
Figure 2. The magnetic flux path diagram of IDRTPMDM. 1. Main flux path of TRPM; 2. Magnetic circuit formed by two RRPMs and TRPM; 3. Leakage flux of TRPM; 4. Leakage flux of SRPM; 5. leakage flux of RRPM.
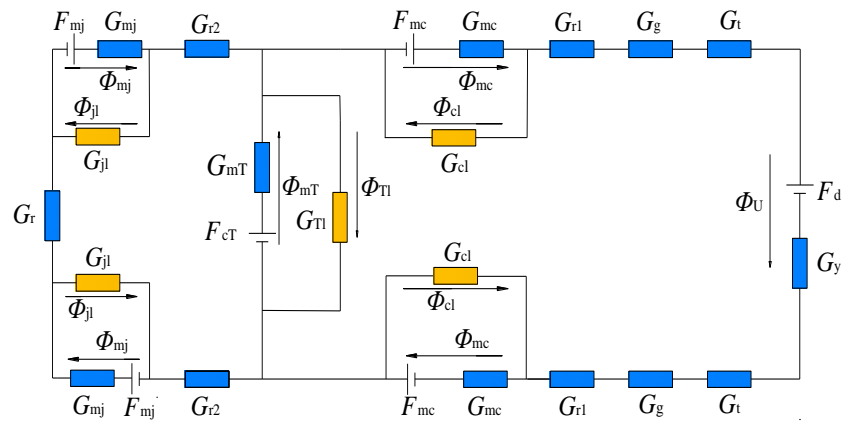

Figure 3. EMC model diagram of IDRTPMDM.

In Figure 2, label 1 is the main flux path of TRPM, label 2 is a closed magnetic circuit formed by two RRPMs and TRPM, label 3 is the leakage flux of TRPM, label 4 is the leakage flux of SRPM, and label 5 is the leakage flux of RRPM.

As shown in Figure 3, F_{cT} is the magnetomotive force provided by TRPM; F_{mj} is magnetomotive force provided by RRPM; F_d is the d-axis component of armature reaction; F_{mc} is the magnetomotive force provided by SRPM; G_{mT} is the equivalent permeability of TRPM; G_{mj} is the equivalent permeability of RRPM; G_{mc} is the equivalent permeability of SRPM; G_{r1} is the equivalent permeability of rotor core between SRPM and RRPM. G_{r1} is the equivalent permeability between the rotor core and the air gap between the rotor and stator. G_r is the equivalent permeability of rotor core between two RRPMs; G_g is the air gap equivalent permeability of permanent magnet drive motor; G_t is the permeability of stator tooth; G_y is the permeability of stator yoke; G_{cl} is the leakage permeability of SRPM; G_{Tl} is the leakage permeability of TRPM; G_{jl} is the leakage permeability of RRPM; Φ_{mT} provides the magnetic flux for TRPM; Φ_{mj} provides the magnetic flux for RRPM; Φ_{Tl} is the leakage flux of TRPM; Φ_{jl} is the leakage flux of RRPM. Φ_U is the no-load effective magnetic flux passing through the air gap.

According to the equivalent magnetic circuit model of IDRTPMDM, the following equations can be obtained from Kirchhoff's law and Ohm's law of magnetic circuit:

$$\begin{cases} 2\phi_{mj} + \phi_{mT} + 2\phi_{mc} = \phi_{jl} + \phi_{Tl} + \phi_{cl} + \phi_{U} \\ (2\phi_{mj} - \phi_{jl})\frac{2}{G_{r3}} + F_{mT} = \phi_{jl}\frac{1}{G_{jl}} \\ F_{mT} = \phi_{mT}\frac{1}{G_{mT}} + \phi_{Tl}\frac{1}{G_{Tl}} \\ F_{mj} = \phi_{mj}\frac{2}{G_{mj}} + \phi_{jl}\frac{1}{G_{jl}} \\ F_{mc} = \phi_{mc}\frac{2}{G_{mc}} + \phi_{cl}\frac{1}{G_{cl}} \\ \left[(2\phi_{mj} - \phi_{jl}) + \phi_{mT} + 2\phi_{mc}\right]\frac{2}{G_{mc}} + \phi_{cl}\frac{1}{G_{cl}} = \phi_{Tl}\frac{1}{G_{Tl}} \\ \phi_{U}(\frac{2}{G_{r1}} + \frac{2}{G_{g}} + \frac{2}{G_{t}} + \frac{1}{G_{y}}) + F_{d} = \phi_{cl}\frac{1}{G_{cl}} \end{cases} \tag{1}$$

Formula, $G_{mj} = \mu_1 \frac{S_{mj}}{b_{mQ}}$; $G_{mT} = \mu_1 \frac{S_{mT}}{b_{mT}}$; $G_{mc} = \mu_1 \frac{S_{mc}}{b_{mc}} = \mu_1 \frac{2R_2 L_a}{(R_1 - R_2)}$. Where R_2 is the outer diameter of the SRPM; R_1 is the inner diameter of the SRPM. The initial size parameters of the rotor poles are determined through the EMC model.

4. Structure Optimization

4.1. Optimization of Rectangular Magnetic Pole Parameters Based on Taguchi Method

For the interior combined magnetic pole permanent magnet drive motor, the size parameters and implantation depth of the permanent magnet have a great influence on the output characteristics of the motor [24]. Therefore, in this paper the peak value of cogging torque (T_{cog}), peak value of air gap magnetic flux density (G_{Bg}) and distortion rate of no-load back electromotive force waveform (K_r) are taken as indicators, and the thickness of TRPM (h_{mT}), the magnetic direction width of TRPM (b_{mT}), the thickness of RRPM (h_{mQ}), and the magnetic direction width of RRPM (b_{mQ}) are taken as indicators. The implantation depth of RRPM (b) is optimized for the parameter. Four factor levels are selected for each parameter. The rectangular magnetic pole optimization parameters and factor level task table are shown in Table 2.

Table 2. Task table of magnetic pole optimization parameters and factor level of rotor.

Parameter	b_{mT}/mm	h_{mT}/mm	b_{mQ}/mm	h_{mQ}/mm	b/mm
Level 1	20	2	5	1	25
Level 2	21	3	6	2	20
Level 3	22	4	7	3	15
Level 4	23	5	8	4	10

The formula for calculating the waveform distortion of the no-load back electromotive force of a new type of permanent magnet drive motor, such as Formula (2)

$$K_r = \frac{\sqrt{U_2^2 + U_3^2 + U_4^2 \cdots\cdots U_N^2}}{U_1} \times 100\% \tag{2}$$

where, U_N—the amplitude of the Nth harmonic in the back electromotive force.

According to factors and level numbers, the experimental matrix with the expression $L_{16}(4^5)$ is established. If the optimization method with a single variable and single indicator is adopted, $4^5 = 1024$ experiments are required, which requires a lot of working time. By using Taguchi's rule, the multi-objective optimization design of the rotor magnetic pole can be completed only after 16 experiments. The orthogonal experimental matrix of parameter influence factors is established, and the results are solved by the finite element method. Orthogonal experimental matrix and calculation results are shown in Table 3.

Table 3. Orthogonal experimental matrix and calculation results. (Reprinted from Ref. [26]).

Order	Experimental Matrix					K_r	T_{cog}	G
	h_{mT}/mm	b_{mT}/mm	h_{mQ}/mm	b_{mQ}/mm	b/mm	%	N·m	T
1	1	1	1	1	1	47.1	0.58	0.51
2	1	2	2	2	2	40.2	0.81	0.63
3	1	3	3	3	3	36.2	1.04	0.74
4	1	4	4	4	4	31.4	1.32	0.83
5	2	1	2	3	4	45.3	0.75	0.58
6	2	2	1	4	3	41.8	0.85	0.62
7	2	3	4	1	2	35.8	1.12	0.80
8	2	4	3	2	1	31.4	1.29	0.82
9	3	1	3	4	2	43.1	1.04	0.69
10	3	2	4	3	1	39.3	1.37	0.79
11	3	3	1	2	4	36.2	1.17	0.75
12	3	4	2	1	3	30.5	1.16	0.81
13	4	1	4	2	3	42.6	1.22	0.74
14	4	2	3	1	4	40.4	1.46	0.80
15	4	3	2	4	1	35.8	1.17	0.76
16	4	4	1	3	2	31.4	1.33	0.84

Use Formula (3) to calculate the finite element simulation analysis results in Table 3:

$$M_{(S)} = \frac{1}{n}\sum_{i}^{n} S_i = \frac{1}{16}\sum_{i=1}^{16} S_{(i)} \tag{3}$$

In the formula, *n* is the test's number; *i* is a constant, *i* = 1, 2, 3... n; S_i is the average target performance value for the *i*th test.

The average value of the specific target performance is calculated for the factor level of each parameter, such as Formula (4)

$$M_{xi} = \frac{1}{4}[M_x(j) + M_x(k) + M_x(l) + M_x(n)] \tag{4}$$

where M_{xi} is the average value of the performance index under the ith influence factor of parameter *x*; M_x is the performance index of parameter *x* under a certain experiment; *J*, *k*, *l*, *n* are experimental numbers.

In order to express the data more intuitively, the change of each optimization parameter with the performance parameter is represented by a bar graph [26], as shown in Figures 4–6.
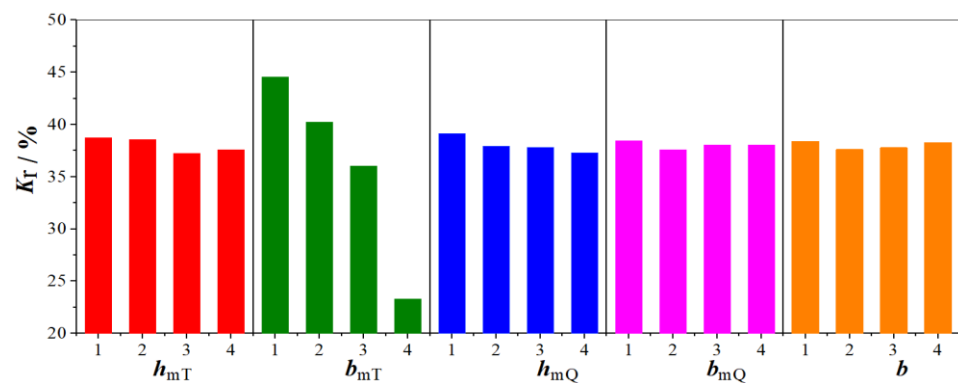
Figure 4. The influence of various factors on *Kr*. (Adapted from Ref. [26]).
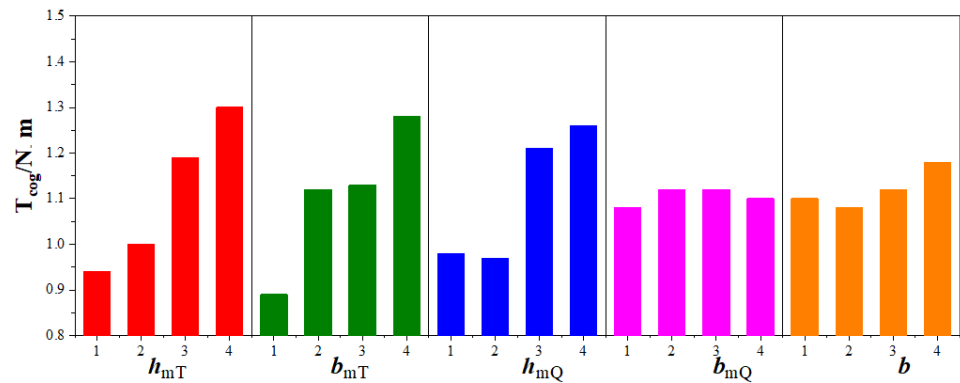
Figure 5. The influence of various factors on T_{cog}. (Adapted from Ref. [26]).
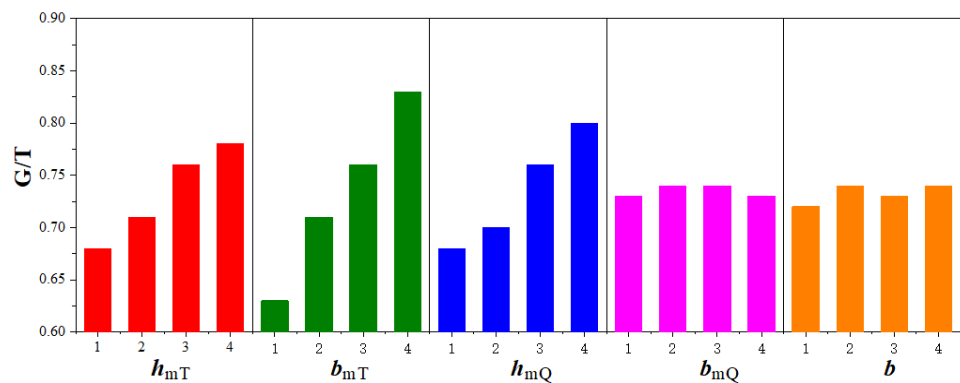

Figure 6. The influence of various factors on *G*. (Adapted from Ref. [26]).

From the above three graphs, it can be seen that these three horizontal combinations are designed for the optimization of individual performance indicators. If the impact of the three performance indicators on the motor is comprehensively considered, variance analysis is required to further analyze the impact of the change of parameters on different indicators, the proportion of the impact of the change of each parameter on its indicators is determined, so as to obtain the optimization results. The variance is calculated as follows:

$$S_{(s)} = \frac{1}{z}\sum_{i=1}^{z}\left[M_{xi} - M_{(s)}\right]^2 \tag{5}$$

where, *s* is the influencing factor, such as b_1, h_1, b_2, h_2, b; $S(s)$ is variance of a performance indicator under parameter s; Z is number of levels of each parameter; $M_{(s)}$ is the average value of a certain performance indicator. The calculation results of $S_{(s)}$ are shown in Table 4.

Table 4. Variance value and proportion of each parameter performance index at four levels. (Reprinted from Ref. [26]).

Parameter	S_{kr}		S_T		S_G	
	Variance	Proportion%	Variance	Proportion%	Variance	Proportion%
h_{mT}	0.396	0.85	0.0210	23.28	0.0016	16.50
b_{mT}	24.760	53.65	0.0180	19.96	0.0053	54.64
h_{mQ}	20.743	45.00	0.0490	54.32	0.0020	20.62
b_{mQ}	0.116	0.35	0.0003	0.33	0.00005	0.51
b	0.072	0.15	0.0019	2.11	0.00075	7.73
Total value	46.087	100	0.0902	100	0.00970	100

From Table 4, it can be seen that the variance value can intuitively reflect the proportion of the impact of changes in various optimization parameters on performance indicators.

The parameter with the highest proportion of influence on the peak value of magnetic flux of the air gap is b_{mT}. The width of TRPM h_{mT} has a greater influence on the cogging torque for IDRTPMDM. The performance index that has the greatest influence on the thickness of magnetization direction b_{mQ} and implantation depth b of RRPM is the peak value of air gap magnetic flux density. Based on the above analysis, the selection of factor levels should be optimized based on the minimum distortion rate, maximum peak air gap magnetic flux density, and minimum peak cogging torque of the no-load back electromotive force waveform. In summary, the optimal design variable combination is finally determined as h_{mT} (1) b_{mT} (4) h_{mQ} (1) b_{mQ} (3) b (2).

4.2. Optimization of Semi-Circular Magnetic Pole Parameters Based on Response Surface Methodology

The IDRTPMDM proposed in this paper adopts a single-layer winding distribution wiring mode, stator structure and rotor pole parameters. On this basis, in order to fully utilize the limited rotor space, increase the number of layers of permanent magnets, improve the salient pole rate of the permanent magnet drive motor, and reduce magnetic leakage, the semi-circular radial permanent magnet is embedded in the d axis magnetic circuit of the rotor magnetic pole. In the design of traditional permanent magnet drive motors, the thickness in the magnetization direction of permanent magnets is generally designed to be thicker to avoid irreversible demagnetization of permanent magnets. However, if the thickness in the magnetization direction is too thick, the d-axis reluctance will be increased and the d-axis inductance will be reduced, which is not good for broadening the efficient range of permanent magnet drive motors. When the motor is loaded, the stator winding needs to pass a large armature current to increase the output torque, but the larger armature current will increase the probability of irreversible demagnetization of the permanent magnet. In conclusion, in order to enhance the magnet flux concentration effect, demagnetization resistance and output torque performance of the air gap magnetic field, it is important to optimize the size of the semi-circular radial permanent magnet. Since the parameters of the magnetic poles of TRPM and RRPM have been determined, the inner and outer radius of the semi-circular radial permanent magnet and the implantation depth in the rotor core is restricted by the magnetic pole size of the rotor. Therefore, the constraint relationship can be designed and optimized for the dimensional parameters of the semi-circular radial permanent magnet, as shown in Figure 7.
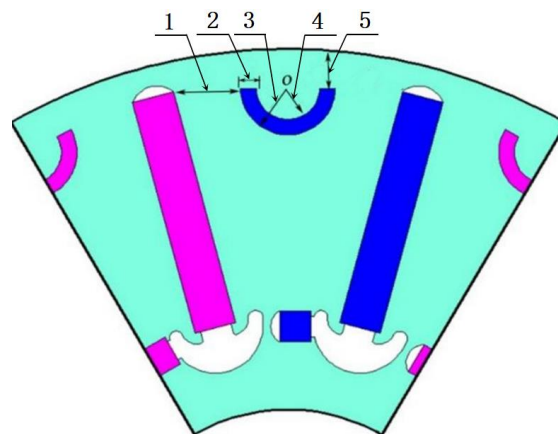

Figure 7. Dimension constraints of semi-circular radial magnetic field permanent magnet. 1. Distance between TRPM and SRPM (d_t); 2. Thickness of SRPM (t); 3. Outer radius of SRPM (R_1); 4. Inter radius of the SRPM (R_2); 5. The implantation depth of SRPM.

From Figure 7, the center of SRPM is O, and the distance d from the center O to the outer diameter of the rotor is the implantation depth of the SRPM. In order to keep rotor structural integrity when the motor is running at high speed, the implantation depth of the permanent magnet should not be less than 2 mm, and outer radius of SRPM is

R_1 and the inner radius of SRPM is R_2. The difference between the two is equal to the thickness t in the magnetization direction of SRPM, which faces the air gap. In order to prevent irreversible demagnetization, the thickness in the magnetization direction should be greater than 2 mm. In order to avoid magnetic circuit saturation in the circular arc and prevent the magnetic flux from being generated to the air gap, the internal radius of SRPM R_2 should not be less than 2 mm, and the distance between TRPM and RRPM is d_t. In order to meet the mechanical strength of the rotor punching and avoid the excessive saturation of the magnetic circuit, d_t should be greater than or equal to 3 mm, and the radial distance between SRPM and the rectangular permanent magnet should be greater than 5 mm. Because each pole radian of the motor is 30°, minus 5.5° of the pole radian corresponding to 5 mm, according to the geometric relationship in the figure, its dimension constraint equation can be established.

$$\begin{cases} 2 \le R_1 - R_2 = t \le 3 \\ 2 \le R_2 < R_1 \\ R_2 + 2 \le R_1 \le d_t + R_1 \\ d \ge 2 \\ d + r_1 + 5 \le 20 \\ d_t \ge 3 \\ 2(d_t + r_1) = (D_r - 2)\sin\theta/2 \end{cases} \tag{6}$$

According to the geometric dimension relationship between the combined magnetic poles of the rotor, the range of values for the three position size parameters of SRPM can be determined as shown in Formula (7).

$$\begin{cases} 5\,\text{mm} \le R_1 \le 8\,\text{mm} \\ 2\,\text{mm} \le t \le 3\,\text{mm} \\ 2\,\text{mm} \le d \le 7\,\text{mm} \end{cases} \tag{7}$$

In order to further reveal the mechanism by which the magnetic pole parameters of SRPM affect motor performance, the function of SRPM in this paper is to improve the air gap magnetic density and make up for the depression in the back electromotive force waveform. The internal radius of the SRPM is set as R_1, the thickness of SRPM t and the implantation depth d as experimental factors, and the peak value of air gap magnetic density is set as Y_1. The waveform distortion of the air gap magnetic density Y_2 as a response value; the calculation formula for Y_2 is shown in Formula (8).

$$Y_2 = \frac{\sqrt{B^2_{\delta 2} + B^2_{\delta 3} + B^2_{\delta 4} \cdots\cdots + B^2_{\delta n}}}{B_{\delta 1}} \times 100\% \tag{8}$$

According to the CCD (Central composite design) test scheme of the response surface method, the relationship equation between the response value and the independent variable is established by using the least square method and the regression model variance analysis:

$$\begin{aligned} Y_1 = {} & 1.28 + 0.052R_1 + 0.042t + 0.048d - 0.082R_1t + 0.076R_1d \\ & + 0.062td - 0.16R_1^2 + 0.016t^2 + 0.033d^2 \end{aligned} \tag{9}$$

$$\begin{aligned} Y_2 = {} & 52.17 - 0.015R1 + 0.14t + 1.54d - 0.2R1t + 0.36R1d \\ & + 0.019td + 0.26R_1^2 + 0.29t^2 - 1.7d^2 \end{aligned} \tag{10}$$

According to the above Formulas (9) and (10), the magnitude of regression coefficients of each factor in the model can be calculated, and the order of primary and secondary influencing factors affecting Y_1 is as follows: R_1, t, d, and the order of primary and secondary influencing factors affecting Y_2 is as follows: d, t, R_1.

The suitability of the model is confirmed by using the normal graph of the residual, as shown in Figure 8. The residuals subtract the values suitable for the regression model

from the actual measured values. The smaller the residuals, the more accurately the regression model can describe the actual observed results. The data distribution is close to the diagonal, indicating that the distribution of residuals is close to the normal distribution Y_1. By analyzing the residual diagram, it can be concluded that the majority of true values fall on the predicted values, and only a few portion of the true values are distributed around the predicted values, showing that the model fits the actual results well.
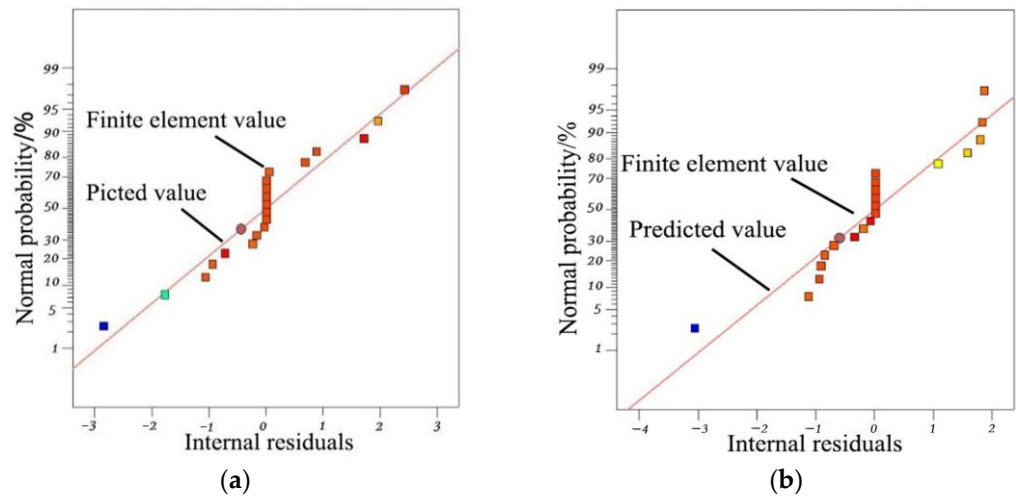
Figure 8. Residual normal distribution map of Y_1 and Y_2: (**a**) Residual normal distribution map of Y_1; (**b**) Residual normal distribution map of Y_2.

The response surface between the outer radius, magnetization direction thickness and implantation depth of the SRPM and peak value of air gap magnetic flux density (Y_1) is established in Figure 9. From the figure, the interaction between the three is very obvious. When t = 2 mm and R_1 changes from 5 mm to 8 mm, the Y_1 first increases and then decreases, as shown in Figure 9a. If the horizontal coordinate of R_1 is fixed at a certain value, Y_1 tends to decrease with the increase in t. According to the contour density and partial regression equation, when the influence of R_1 on the Y_1 is greater than that of d, the value of Y_1 first increases and then decreases, as shown in Figure 9b. If fixed, the horizontal abscissa of d at a certain value in Figure 9c, the value of t increases, and the value of Y_1 first decreases and then increases. According to contour distribution and analysis of the partial regression equation, the influence of t on Y_1 is greater than d.
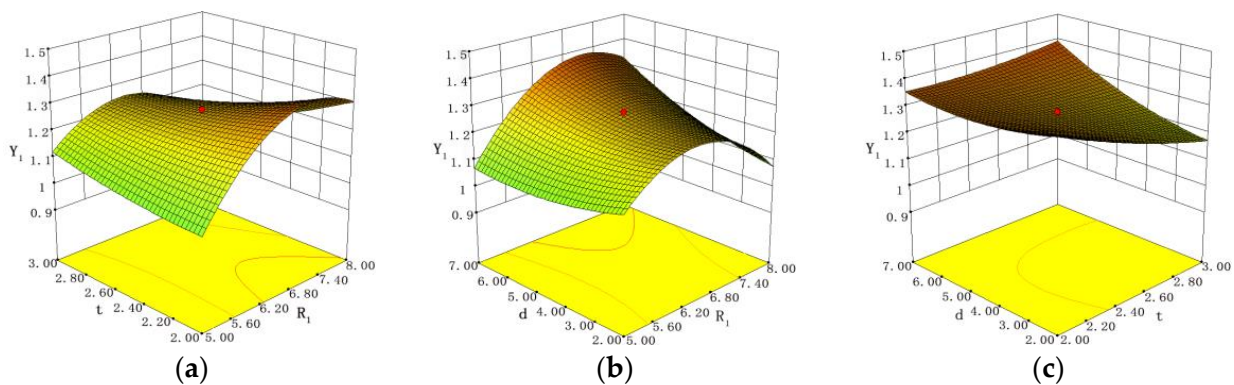

Figure 9. Influence surface of interaction on Y_1: (**a**) Interaction between R_1 and t; (**b**) Interaction between R_1 and d; (**c**) Interaction between t and d.

The response surface of the outer radius of SRPM, magnetization direction thickness and the implantation depth to the waveform distortion of the air gap magnetic density (Y_2) is established as shown in Figure 10. As shown in Figure 10a, when t = 2 mm and R_1 changes from 5 mm to 8 mm, the value of Y_2 decreases first and then increases. When R_1 is

a constant value, the value of Y_2 increases with t. According to the contour density and partial regression equation, the influence of t on the Y_2 is greater than that of R_1. When d = 2 mm and X_1 changes from 5 mm to 8 mm, the value of Y_2 decreases first and then increases, as shown in Figure 10b. The horizontal coordinate of R_1 is fixed at a certain value as the value of d increases, the waveform distortion rate of air gap magnetic flux density first increases and then decreases, as shown in Figure 10c. According to the contour density cloud map and partial regression equation, the influence of d on the Y_2 is greater than that of d. When d = 2 mm and t changes from 2 mm to 3 mm, the value of Y_2 shows a trend of decreasing first and then increasing. The horizontal coordinate of d is fixed at a certain value, with the increase in t, the Y_2 gradually increases. Based on the contour density cloud map and partial regression equation, t has a greater influence on Y_2 than d.

(a)   **(b)**   **(c)**
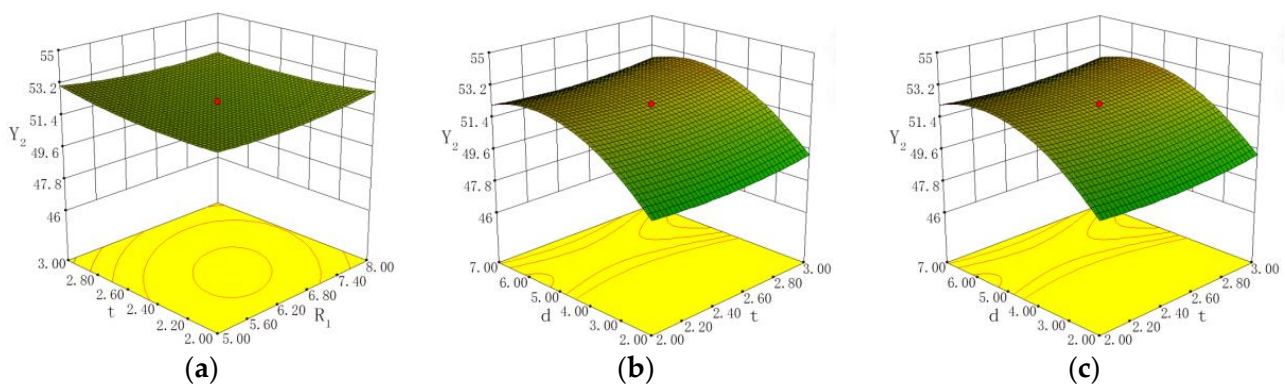
Figure 10. Surface effect of interaction factors on Y_2: (**a**) Interaction between R_1 and t; (**b**) Interaction between R_1 and d; (**c**) Interaction between t and d.

Finally, the rotor pole parameters of the IDRTPMDM can be determined, as shown in Table 5.

Table 5. Structural parameters of IDRTPMDM.

Parameter	Before Optimization/mm	After Optimization/mm
h_{mT}	4	5
b_{mT}	23	20
h_{mQ}	3	2
b_{mQ}	6	5
b	25	20
R_1	7	6.2
t	2	2.4
d	3	2

5. Finite Element Verification

In order to verify the superiority of the optimized IDRTPMDM, the results of the initial rotor pole calculated by the EMC method and the optimal design obtained by Taguchi and the response surface method are compared. Based on the above optimization, the stator structure, winding configurations, rotor outside diameter, silicon steel sheet (DW310-50) and permanent magnet material (NeFeB 35) are the same before and after the permanent magnet drive motor, the EMC calculation results and optimization results are simulated and verified using finite element software (Ansys Maxwell 2021, Ansys Inc., Canonsburg, PA, USA). The simulation analysis results of magnetic field lines and flux density of IDRTPMDM before and after optimization are shown in Figure 11. The upper half of Figure 11a,b shows the simulation results of magnetic field lines, it can be seen that the trend of magnetic field lines before optimization is not uniform with large magnetic leakage. After optimization, the distribution of magnetic field lines is uniform, and the magnetic leakage is reduced. In addition, the magnetic field line trend obtained from

finite element simulation analysis is basically consistent with the EMC analysis results. The lower half of Figure 11a,b shows the simulation results of magnetic flux density; the distribution of magnetic flux density before the optimization is not uniform, and the saturation phenomenon occurs in many places. Moreover, the magnetic flux density in the stator part is significantly lower than that of the optimized motor, indicating that there is less magnetic flux passing through the air gap and lower magnetic flux density in the air gap.

(a) **(b)**
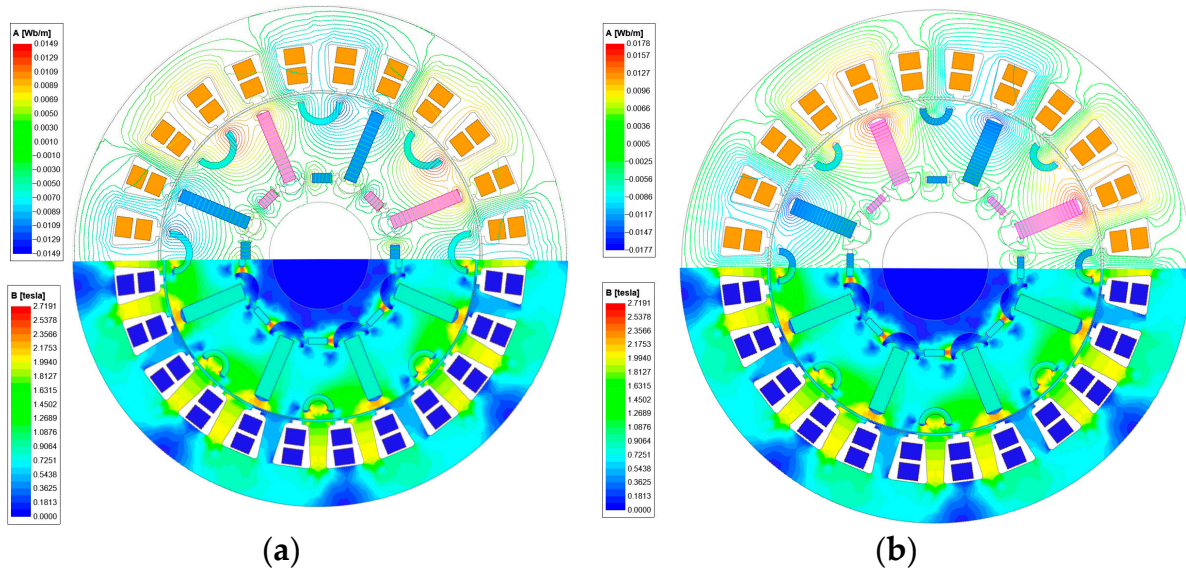
Figure 11. Magnetic field lines and flux density distribution of IDRTPMDM: (**a**) Magnetic field lines and flux density distribution before optimization; (**b**) Magnetic field lines and flux density distribution after optimization.

The no-load back electromotive force waveform of IDRTPMDM in one cycle before and after optimization is shown in Figure 12. The no-load back electromotive force waveform before optimization has obvious depression, and the optimized back electromotive force is more similar to sine, indicating that the optimized rotor pole magnetic leakage is less, and the magnetic accumulation effect is more obvious.
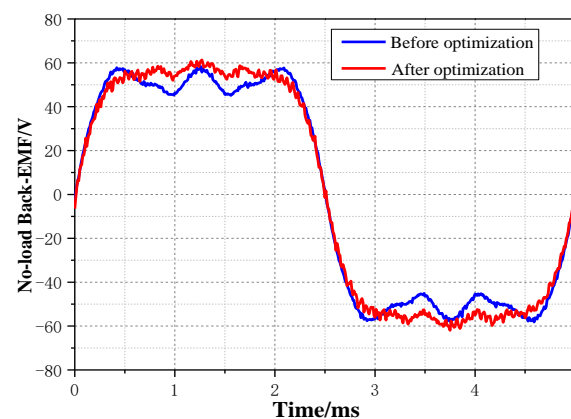
Figure 12. The waveform of no-load back-EMF.

By comparing the amplitude of harmonic frequency of the no-load back electromotive force of the permanent magnet drive motor before and after optimization, the amplitude of the fundamental wave before optimization is 36.77 V and the waveform distortion rate of back electromotive force is 45%. After optimization, the fundamental amplitude is 38.63 V and the waveform distortion rate of back electromotive force is 33%, as shown in Figure 13.
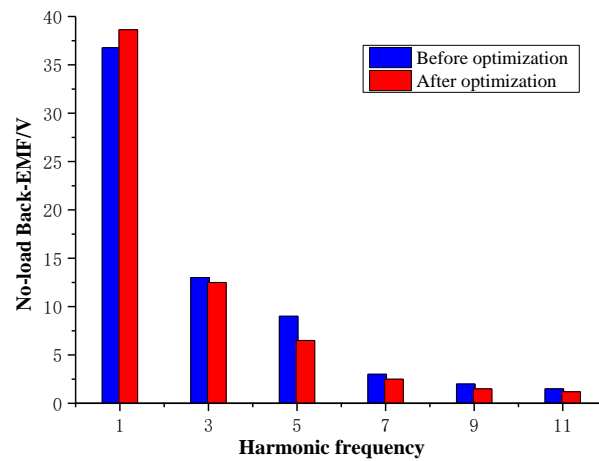
Figure 13. Harmonic content of no-load back-EMF.

The finite element simulation results of the cogging torque of IDRTPMDM are shown in Figure 14. It can be seen that the peak value of cogging torque after optimization decreases from 1.12 N·m to 0.55 N·m, reducing by about 51%, which verifies the correctness of the optimization method.
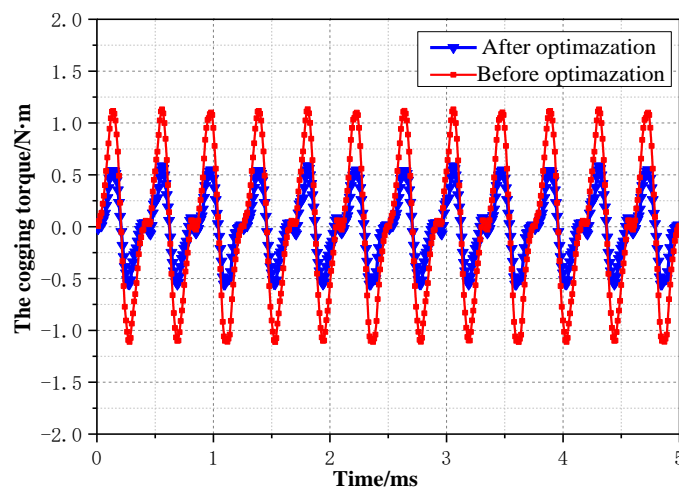

Figure 14. Cogging torque before and after optimization.

Figure 15 shows the surface graph of the no-load air gap flux density within a magnetic pole range as a function of the rotor axis and circumferential direction. The optimized no-load air gap magnetic flux density is closer to a sine wave, with a maximum air gap flux density of 1.22 T, while the maximum air gap flux density before optimization is 0.82 T, indicating that under the optimal parameter combination, the leakage magnetic flux rate of the rotor pole is reduced; the utilization rate of the permanent magnet material is higher and the air gap flux density of IDRTPMDM is significantly improved.

Figure 16a,b shows the efficiency map of IDRTPMDM under different output characteristics before and after optimization. Through comparison, it can be found that the optimized motor not only has high efficiency but also has a wider range of efficient working areas (areas with efficiency greater than 85%). Obviously, the motor has a wider efficiency range in Figure 16b, which can extend the range of electric vehicles.
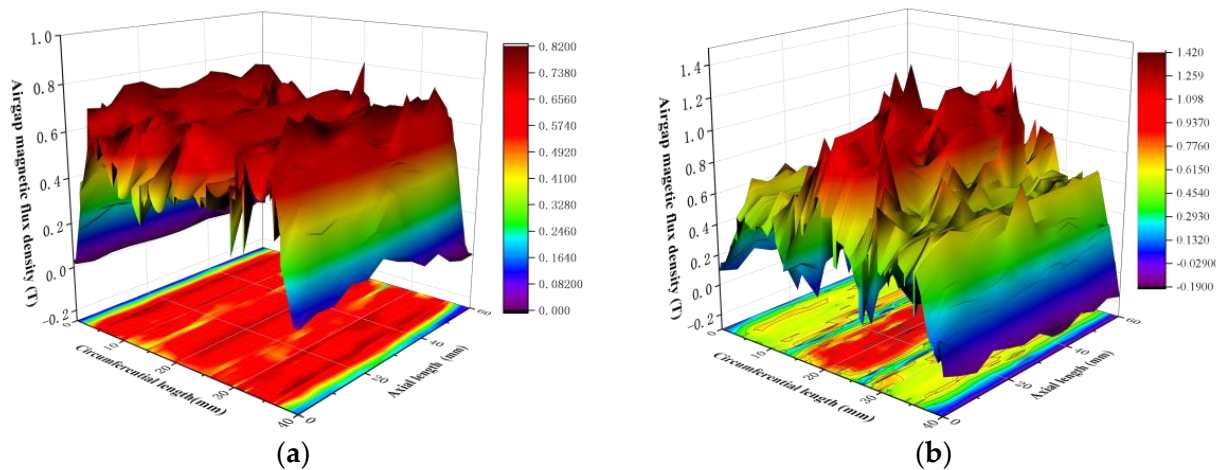
Figure 15. Distribution map of air gap flux density before and after optimization: (**a**) Distribution of air gap flux density before optimization; (**b**) Distribution of air gap magnetic flux after optimization.
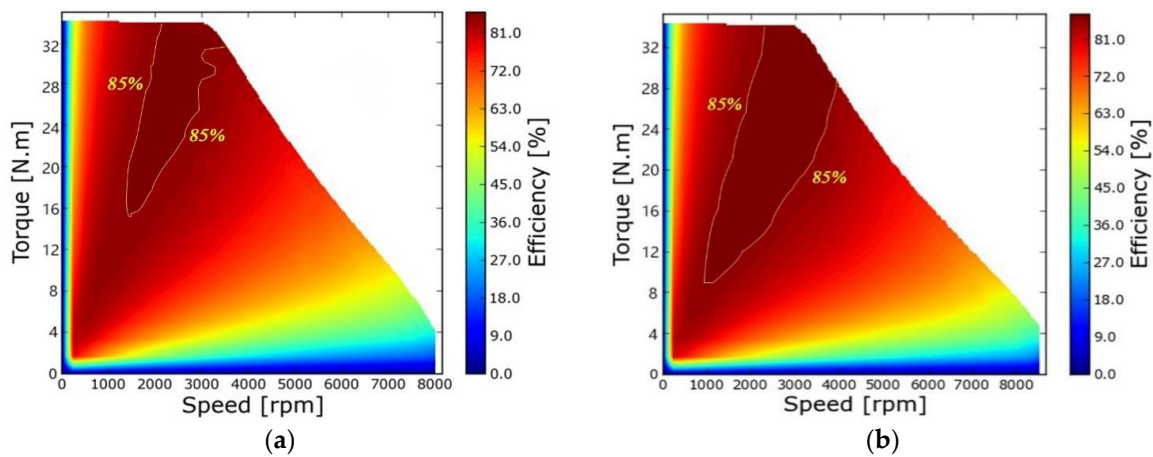

Figure 16. Efficiency map before and after optimization: (**a**) The diagram of efficiency map before optimization; (**b**) The diagram of efficiency map after optimization.

6. Experimental Testing of IDRTPMDM

In order to verify the correctness of the above theoretical calculation and simulation analysis, this article has developed a prototype based on the optimized parameters of the magnetic pole, such as Figure 17, and the test bench is shown in Figure 18.
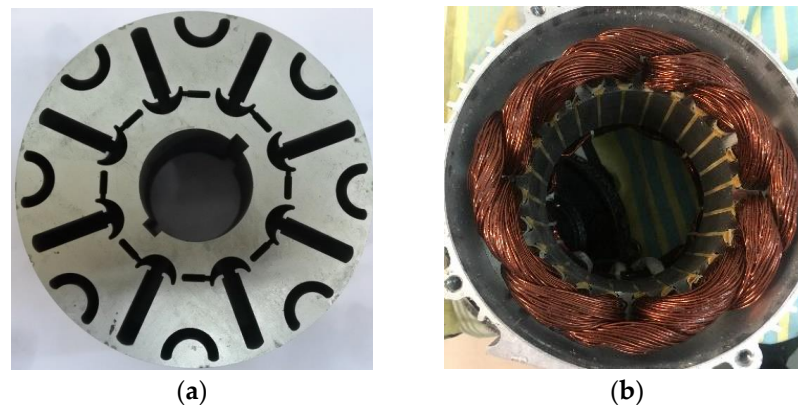
Figure 17. The diagram of prototype: (**a**) Rotor structure diagram; (**b**) Stator structure diagram.
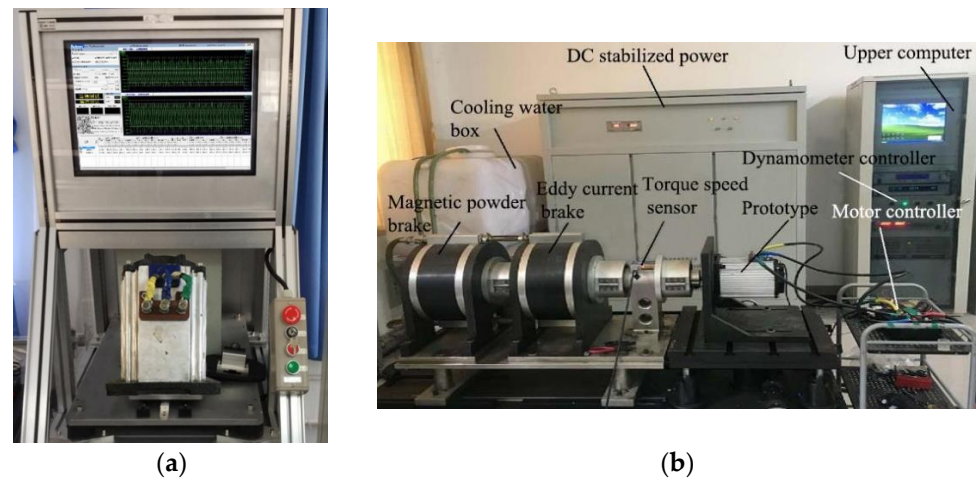
Figure 18. The diagram of test platform: (**a**) Test bench for cogging torque; (**b**) Motor dynamometer test bench.

Then this article developed a testing plan for the motor output characteristics [27,28], Figure 19 shows the three-phase no-load back electromotive force test waveform and finite element analysis results at 3000 r/min. The effective value of the test waveform of the back electromotive force is about 60 V, and close to the sine wave. Compared with Figure 12, the simulation result of the back electromotive force is 59 V, this is because the motor loses more energy during actual testing, such as the influence of assembly accuracy or motor temperature. The experimental results of the relationship between back electromotive force and speed change are shown in Figure 20. The finite element calculation results are basically consistent with the experimental test results.
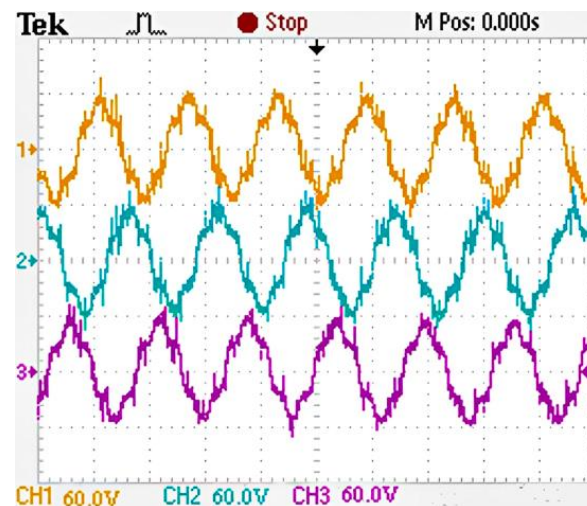

Figure 19. The measured waveform of prototype.

In this paper, the motor dynamometer test bench (Figure 18b) is used to test the Mechanical characteristic curve of the IDRTPMDM, as shown in Figure 21. The optimized motor has a wide magnetic weakening range and a large output torque, which can ensure an output power of 3 kW at 3000 r/min. The simulation results have a high fit with the test results below 4000 r/min, but as the speed increases, the numerical difference between the finite element simulation results and the measured results gradually increases. The reason is that as speed increases, wind friction and mechanical losses increase, leading to an increase in calculation errors. However, the consistency between the two is still high.
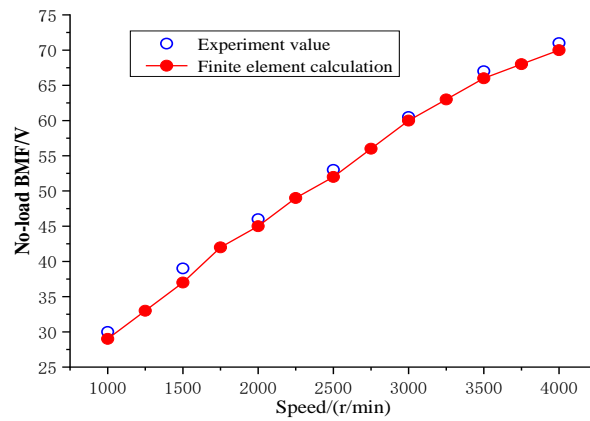
**Figure 20.** The test curve of no-load BMF with motor speed.
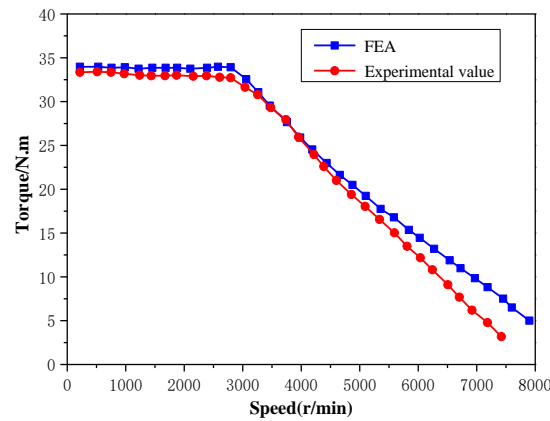
Figure 21. Mechanical characteristic curve of the prototype.

The cogging torque of IDRTPMDM can be tested using the instrument shown in Figure 18a, the result is shown in Figure 22. The maximum value measured in the experiment is 0.58 N·m. The maximum obtained from the previous simulation analysis is 0.55 N·m, the difference between the two is caused by machining errors during the prototype manufacturing process, but within a reasonable range, this also verifies the correctness and accuracy of the previous theoretical analysis.
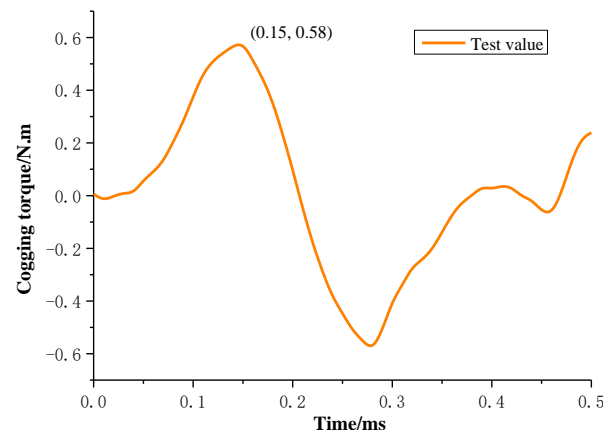

Figure 22. Experimental test results of cogging torque.

7. Conclusions

This paper proposes a new type of IDRTPMDM to improve the output performance of electric vehicle drive systems. Based on the complex structure of the motor, an EMC

model is established, and the result of EMC calculation as the initial parameter, then a combination of the orthogonal experimental method and the response surface method is proposed which can quickly, efficiently, and accurately obtain motor parameter values. The results before and after optimization are verified by finite element simulation, the waveform of the no-load BMF of the motor is more like the sine wave after optimization. After Fourier decomposition, the fundamental wave amplitude increases from 36.77 V before optimization to 38.63 V, and the distortion rate of no-load BMF decreases from the original 45% to 33%. The no-load air gap magnetic density increased from 0.82 T before optimization to 1.22 T after optimization. The cogging torque is reduced by about 51%, and the optimized motor has a wider efficiency interval, which is more in line with the output characteristics of the drive motor for electric vehicles. Finally, a prototype is made and experimentally tested; the results are basically consistent with the theoretical analysis, indicating that the optimization method in this paper is correct, thus verifying the effectiveness of the proposed multi-objective optimization algorithm. The paper provides a new method for optimizing interior combined pole permanent magnet motors.

Author Contributions: Methodology, S.M.; Software, S.M. and K.C.; Validation, S.M. and Q.Z.; Formal analysis, Q.Z.; Data curation, K.C.; Writing—original draft, S.M. and Q.Z.; Writing—review and editing, Q.Z. and S.M.; Supervision, S.M. All authors have read and agreed to the published version of the manuscript.

Data Availability Statement: The data presented in this study are available on request from the corresponding author. The data are not publicly available because they are part of ongoing research.

Conflicts of Interest: The authors declare no conflict of interest.

References

1. Husain, T.; Hasan, I.; Sozer, Y.; Husain, I.; Muljadi, E. Cogging Torque Minimization in Transverse Flux Machines. *IEEE Trans. Ind. Appl.* **2019**, *55*, 385–397. [CrossRef]
2. Lee, Y.-H.; Hsieh, M.F.; Chen, P.-H. A Novel Variable Flux Spoke Type Permanent Magnet Motor With Swiveling Magnetization for Electric Vehicles. *IEEE Access* **2022**, *10*, 62194–62209. [CrossRef]
3. Jung, H.-C.; Kim, D.-J.; Jung, S.-Y.; Lee, D. Optimization Method to Maximize Efficiency Map of a Drive Motor With Electrical Winding Changeover Technique for Hybrid EV. *IEEE Trans. Appl. Supercond.* **2020**, *30*, 5205405. [CrossRef]
4. Cui, W.; Wang, D.; Ren, L.; Zhang, Y. A New Optimized IPMSM for EVs With Reduced Magnet Loss for Over-Modulation Operation. *IEEE Trans. Magn.* **2023**, *59*, 8200104. [CrossRef]
5. Yu, Y.; Pei, Y.; Chai, F.; Doppelbauer, M. Performance Comparison Between Permanent Magnet Synchronous Motor and Vernier Motor for In-Wheel Direct Drive. *IEEE Trans. Ind. Electron.* **2023**, *70*, 7761–7772. [CrossRef]
6. Sun, X.; Shi, Z.; Lei, G.; Guo, Y.; Zhu, J. Analysis and Design Optimization of a Permanent Magnet Synchronous Motor for a Campus Patrol Electric Vehicle. *IEEE Trans. Veh. Technol.* **2019**, *68*, 10535–10544. [CrossRef]
7. Zhu, X.; Huang, J.; Quan, L.; Xiang, Z.; Shi, B. Comprehensive Sensitivity Analysis and Multiobjective Optimization Research of Permanent Magnet Flux-Intensifying Motors. *IEEE Trans. Ind. Electron.* **2019**, *66*, 2613–2627. [CrossRef]
8. Wang, D.; Peng, C.; Li, J.; Wang, C. Comparison and Experimental Verification of Different Approaches to Suppress Torque Ripple and Vibrations of Interior Permanent Magnet Synchronous Motor for EV. *IEEE Trans. Ind. Electron.* **2023**, *70*, 2209–2220. [CrossRef]
9. Chen, H.; Demerdash, N.A.O.; El-Refaie, A.M.; Guo, Y.; Hua, W.; Lee, C.H.T. Investigation of a 3D-Magnetic Flux PMSM With High Torque Density for Electric Vehicles. *IEEE Trans. Energy Convers.* **2022**, *37*, 1442–1454. [CrossRef]
10. Zhang, C.; Zhang, C.; Wang, Y.; Wang, Y.; Zhang, H.; Zhang, H.; Wu, Z.; Wu, Z.; Tao, J.; Tao, J.; et al. Armature Reaction on Implementation of Embedded Magnetic Encoder in Fractional-Slot Concentrated-Winding Permanent Magnet Machines. *IEEE Trans. Ind. Electron.* **2023**, *70*, 6699–6710. [CrossRef]
11. Kim, H.; Park, Y.; Oh, S.-T.; Jang, H.; Jung, D.-H.; Jang, I.S.; Lee, J. Study on Analysis Method of Asymmetric Permanent Magnet Assistance Synchronous Reluctance Motor Considering Magnetic Neutral Plane Shift. *IEEE Trans. Appl. Supercond.* **2020**, *30*, 5200904. [CrossRef]
12. Qu, G.; Fan, Y. Design of a New Consequent-Pole Segmented Dual-Stator Permanent Magnet Machine. *IEEE Trans. Magn.* **2022**, *58*, 8103005. [CrossRef]

13. Zheng, M.; Zhu, Z.Q.; Cai, S.; Xue, S.S. A Novel Modular Stator Hybrid-Excited Doubly Salient Synchronous Machine With Stator Slot Permanent Magnets. *IEEE Trans. Magn.* **2019**, *55*, 8104409. [CrossRef]

14. Zhu, X.; Wang, X.; Zhang, C.; Wang, L.; Wu, W. Design and Analysis of a Spoke-Type Hybrid Permanent Magnet Motor for Electric Vehicles. *IEEE Trans. Magn.* **2017**, *53*, 8208604. [CrossRef]

15. Si, J.; Gao, M.; Yang, X.; Gao, C.; Feng, H.; Hu, Y. Feasibility analysis and optimization design of PMSM with 120 degrees phase belts toroidal windings for electric vehicles. *IET Electr. Power Appl.* **2021**, *15*, 1161–1173. [CrossRef]

16. Liu, X.; Zhu, W.; Guo, G.; Liang, J. Optimal design and performance analysis of a variable flux flux-intensifying permanent magnet motor. *Electr. Mach. Control* **2023**, *27*, 120–132+142. [CrossRef]

17. Gao, P.; Sun, X.; Gerada, D.; Gerada, C.; Wang, X. Improved V-shaped interior permanent magnet rotor topology with inward-extended bridges for reduced torque ripple. *IET Electr. Power Appl.* **2020**, *14*, 2404–2411. [CrossRef]

18. Li, F.; Hua, W.; Tong, M.; Zhao, G.; Cheng, M. Nine-phase flux-switching permanent magnet brushless machine for low-speed and high-torque applications. *IEEE Trans. Magn.* **2015**, *51*, 8700204.

19. Chen, Y.; Zhu, X.; Quan, L.; Han, X.; He, X. Parameter sensitivity optimization design and performance analysis of double-salient permanent-magnet double-stator machine. *Trans. China Electrotech. Soc.* **2017**, *32*, 160–168.

20. Orosz, T.; Pánek, D.; Kuczmann, M. Performance analysis of a robust design optimization of a solenoid with different sensitivity metrics. *J. Comput. Appl. Math.* **2023**, *424*, 115021. [CrossRef]

21. Sun, Y.K.; Yuan, Y.; Huang, Y.H.; Hu, W.H.; Xiang, Q.W.; Zhou, Y.H. Multi-objective optimal design of single winding bearingless switched reluctance motor. *J. Mot. Control* **2016**, *20*, 32–39.

22. Hua, Y.; Liu, Y.; Pan, W. Multi-objective Optimization Design of Bearingless Permanent Magnet Synchronous Motor Using Improved Particle Swarm Optimization Algorithm. *Proc. CSEE* **2023**, *43*, 4443–4452. [CrossRef]

23. Chen, Y.; Quan, L.; Zhu, X.; Mo, L. Optimal design and electromagnetic performance analysis of double-salient permanent-magnet double-rotor motors. *Proc. CSEE* **2014**, *34*, 1912–1921.

24. Zhu, X.; Xiang, Z.; Quan, L.; Wu, W.; Du, Y. Multimode optimization design methodology for a flux-controllable stator permanent magnet memory motor considering driving cycles. *IEEE Trans. Ind. Electron.* **2018**, *65*, 5353–5366. [CrossRef]

25. Liu, G.; Wang, Y.; Chen, Q. Multi-Objective Optimization of an Asymmetric V-Shaped Interior Permanent Magnet Synchronous Motor. *Electr. Mach. Control* **2018**, *33*, 385–393. [CrossRef]

26. Ma, S.; Zhang, X.; Du, Q.; Shi, L.; Meng, X. Optimization Design of a New Type of Interior Permanent Magnet Generator for Electric Vehicle Range Extender. *J. Electr. Comput. Eng.* **2019**, *2019*, 3108053. [CrossRef]

27. De Santis, M.; Agnelli, S.; Patanè, F.; Giannini, O.; Bella, G. Experimental Study for the Assessment of the Measurement Uncertainty Associated with Electric Powertrain Efficiency Using the Back-to-Back Direct Method. *Energies* **2018**, *11*, 3536. [CrossRef]

28. Mazali, I.I.; Daud, Z.H.C.; Hamid, M.K.A.; Tan, V.; Samin, P.M.; Jubair, A.; Ibrahim, K.A.; Kob, M.S.C.; Xinrui, W.; Ab Talib, M.H. Review of the Methods to Optimize Power Flow in Electric Vehicle Powertrains for Efficiency and Driving Performance. *Appl. Sci.* **2022**, *12*, 1735. [CrossRef]